LETTER

https://doi.org/10.1038/s41586-018-0163-6

# Rapid recovery of life at ground zero of the end–Cretaceous mass extinction

Christopher M. Lowery[1]*, Timothy J. Bralower[2], Jeremy D. Owens[3], Francisco J. Rodríguez-Tovar[4], Heather Jones[2], Jan Smit[5], Michael T. Whalen[6], Phillipe Claeys[7], Kenneth Farley[8], Sean P. S. Gulick[1], Joanna V. Morgan[9], Sophie Green[10], Elise Chenot[11], Gail L. Christeson[1], Charles S. Cockell[12], Marco J. L. Coolen[13], Ludovic Ferrière[14], Catalina Gebhardt[15], Kazuhisa Goto[16], David A. Kring[17], Johanna Lofi[18], Rubén Ocampo-Torres[19], Ligia Perez-Cruz[20], Annemarie E. Pickersgill[21,22], Michael H. Poelchau[23], Auriol S. P. Rae[9], Cornelia Rasmussen[1], Mario Rebolledo-Vieyra[24], Ulrich Riller[25], Honami Sato[26], Sonia M. Tikoo[27], Naotaka Tomioka[28], Jaime Urrutia-Fucugauchi[20], Johan Vellekoop[7], Axel Wittmann[29], Long Xiao[30], Kosei E. Yamaguchi[31,32] & William Zylberman[33]

**The Cretaceous/Palaeogene mass extinction eradicated 76% of species on Earth[1,2]. It was caused by the impact of an asteroid[3,4] on the Yucatán carbonate platform in the southern Gulf of Mexico 66 million years ago[5], forming the Chicxulub impact crater[6,7]. After the mass extinction, the recovery of the global marine ecosystem—measured as primary productivity—was geographically heterogeneous[8]; export production in the Gulf of Mexico and North Atlantic–western Tethys was slower than in most other regions[8–11], taking 300 thousand years (kyr) to return to levels similar to those of the Late Cretaceous period. Delayed recovery of marine productivity closer to the crater implies an impact-related environmental control, such as toxic metal poisoning[12], on recovery times. If no such geographic pattern exists, the best explanation for the observed heterogeneity is a combination of ecological factors—trophic interactions[13], species incumbency and competitive exclusion by opportunists[14]—and 'chance'[8,15,16]. The question of whether the post-impact recovery of marine productivity was delayed closer to the crater has a bearing on the predictability of future patterns of recovery in anthropogenically perturbed ecosystems. If there is a relationship between the distance from the impact and the recovery of marine productivity, we would expect recovery rates to be slowest in the crater itself. Here we present a record of foraminifera, calcareous nannoplankton, trace fossils and elemental abundance data from within the Chicxulub crater, dated to approximately the first 200 kyr of the Palaeocene. We show that life reappeared in the basin just years after the impact and a high-productivity ecosystem was established within 30 kyr, which indicates that proximity to the impact did not delay recovery and that there was therefore no impact-related environmental control on recovery. Ecological processes probably controlled the recovery of productivity after the Cretaceous/Palaeogene mass extinction and are therefore likely to be important for the response of the ocean ecosystem to other rapid extinction events.**

The recent joint expedition of the International Ocean Discovery Program and International Continental Drilling Program (hereafter, Expedition 364) recovered what is, to our knowledge, the first record of the few hundred thousand years immediately after the impact within the Chicxulub crater. Site M0077, which was drilled into the peak ring of the crater[7] (Extended Data Fig. 1), sampled an approximately 130-m-thick, generally upward-fining suevite (that is, melt-bearing impact breccia) overlying impact melt rocks and fractured granite[17]. The boundary between the suevite and overlying earliest-Palaeocene pelagic limestone is in core 40-1 (Fig. 1), and comprises a 76-cm-thick upward-fining, brown, fine-grained micritic limestone that we term the 'transitional unit'. The lower portion of the transitional unit is laminated below 54-cm core depth and contains no trace fossils (Fig. 1 and Extended Data Fig. 2). The laminations are thin, graded beds with sub-millimetre-scale cross-bedding that indicates bottom currents, and are likely due to the movement of wave energy—including tsunami and/or seiches—in the days after the impact. The fine grain size (primarily clay to silt, with some sand-sized grains concentrated in the graded beds) suggests that much of the material in the transitional unit was deposited from resuspension and settling. The transitional unit is overlain by a white pelagic limestone. The lowermost sample taken in this limestone (34 cm core depth) contains the planktic foraminifer *Parvularugoglobigerina eugubina* (which marks the base of Zone Pα), other foraminifer of the same genus (*P. extensa, P. alabamensis*) and *Guembelitria cretacea*. Because many other species that originate within Zone Pα first appear a few centimetres higher in the section (31–32 cm), we conclude that the base of the limestone lies very near the base of this zone, 30 kyr after the impact[18].

Biostratigraphy and basic assumptions about depositional and crater processes indicate that the transitional unit was deposited between several years and 30 kyr after impact (Fig. 2). To better constrain this, we use the abundance of extraterrestrial $^{3}$He to determine sediment accumulation rates (see Methods). This proxy provides a firm upper limit of 8 kyr for deposition, assuming none of the $^{3}$He is reworked. If even a small amount of $^{3}$He is reworked (which is very likely given the prevalence of reworked microfossils and impact debris), then the transitional unit was deposited in a period of time of less than about

[1]Institute for Geophysics, Jackson School of Geosciences, University of Texas at Austin, Austin, TX, USA. [2]Department of Geosciences, Pennsylvania State University, University Park, PA, USA. [3]Department of Earth, Ocean and Atmospheric Science and National High Magnetic Field Laboratory, Florida State University, Tallahassee, FL, USA. [4]Departamento de Estratigrafía y Paleontología, Universidad de Granada, Granada, Spain. [5]Faculty of Earth and Life Sciences (FALW), Vrije Universiteit Amsterdam, Amsterdam, The Netherlands. [6]Department of Geosciences, University of Alaska Fairbanks, Fairbanks, AK, USA. [7]Analytical, Environmental and Geo-Chemistry, Vrije Universiteit Brussel, Brussels, Belgium. [8]Division of Geological and Planetary Sciences, MS 170-25, California Institute of Technology, Pasadena, CA, USA. [9]Department of Earth Science and Engineering, Imperial College London, London, UK. [10]British Geological Survey, Edinburgh, UK. [11]Biogéosciences Laboratory, Université de Bourgogne-Franche Comté, Dijon, France. [12]UK Centre for Astrobiology, School of Physics and Astronomy, University of Edinburgh, Edinburgh, UK. [13]School of Earth and Planetary Sciences, WA-Organic and Isotope Geochemistry Centre (WA-OIGC), Curtin University, Bentley, Western Australia, Australia. [14]Natural History Museum, Vienna, Austria. [15]Alfred Wegener Institute, Helmholtz Centre of Polar and Marine Research, Bremerhaven, Germany. [16]International Research Institute of Disaster Science, Tohoku University, Sendai, Japan. [17]Lunar and Planetary Institute, Houston, TX, USA. [18]Géosciences Montpellier, CNRS, Université de Montpellier, Montpellier, France. [19]Groupe de Physico-Chimie de l´Atmosphère, L'Institut de Chimie et Procédés pour l'Énergie, l'Environnement et la Santé (ICPEES), Université de Strasbourg, Strasbourg, France. [20]Instituto de Geofísica, Universidad Nacional Autónoma De México, Mexico City, Mexico. [21]School of Geographical and Earth Sciences, University of Glasgow, Glasgow, UK. [22]Argon Isotope Facility, Scottish Universities Environmental Research Centre (SUERC), East Kilbride, UK. [23]Department of Geology, University of Freiburg, Frieburg, Germany. [24]Independent consultant, Cancun, Mexico. [25]Institut für Geologie, Universität Hamburg, Hamburg, Germany. [26]Ocean Resources Research Center for Next Generation, Chiba Institute of Technology, Chiba, Japan. [27]Earth and Planetary Sciences, Rutgers University, New Brunswick, NJ, USA. [28]Kochi Institute for Core Sample Research, Japan Agency for Marine-Earth Science and Technology, Kochi, Japan. [29]LeRoy Eyring Center for Solid State Science, Physical Sciences, Arizona State University, Tempe, AZ, USA. [30]Planetary Science Institute, School of Earth Sciences, China University of Geosciences, Wuhan, China. [31]Department of Chemistry, Toho University, Chiba, Japan. [32]NASA Astrobiology Institute, Mountain View, CA, USA. [33]CNRS, Institut pour la Recherche et le Développement, Aix Marseille University, Marseille, France. *e-mail: cmlowery@utexas.edu

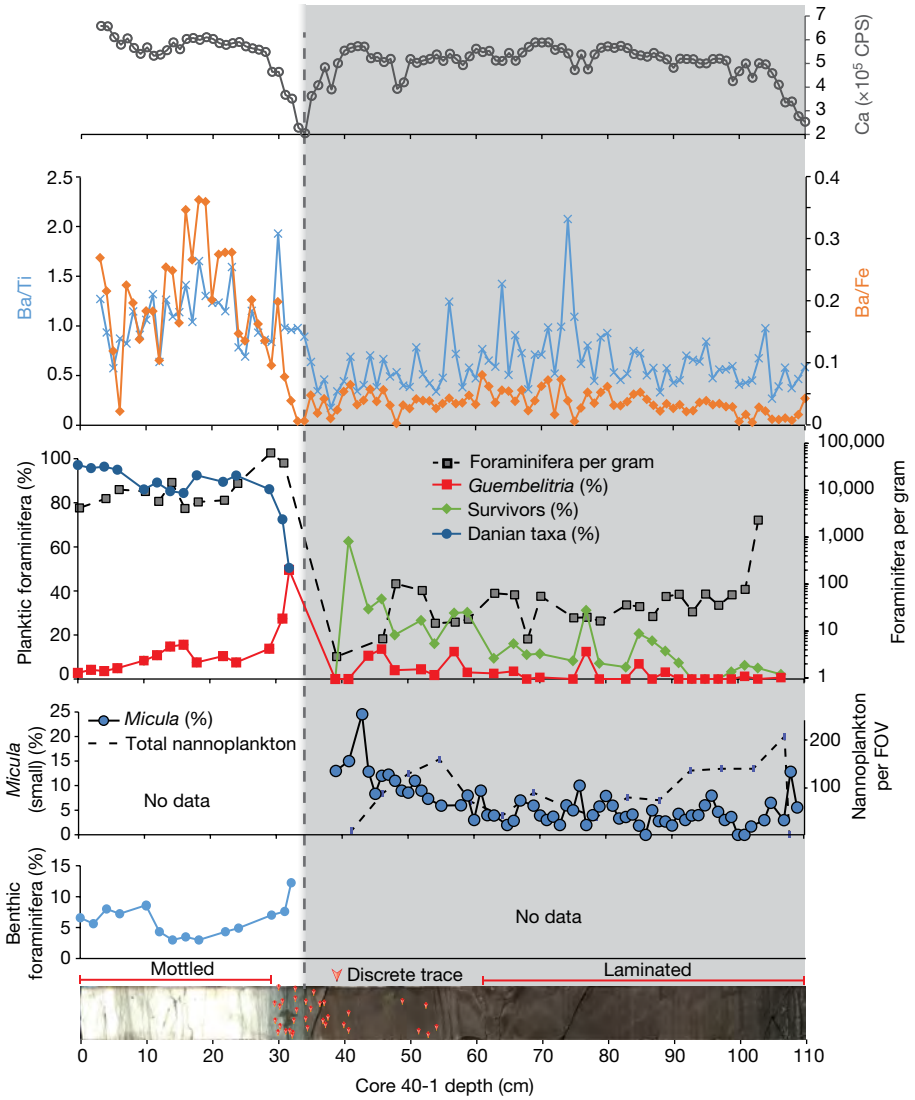


**Fig. 1 | Palaeoproductivity indicators in the earliest Palaeocene at site M0077.** The shaded area is the transitional unit and the dashed line represents the contact with the overlying pelagic limestone. Top to bottom: X-ray fluorescence-derived calcium abundance in counts per second (CPS); Ba/Ti and Ba/Fe ratios; percentage abundances of key planktic foraminiferal groups, including percentage of *Guembelitria*, percentage of survivors (that is, Cretaceous species known to survive the impact) and percentage of Danian taxa (that is, species that evolved after the impact) as a percentage of total foraminifera; foraminifera per gram of sediment, plotted on a logarithmic scale; percentage of *Micula* smaller than 2 μm (against total nannoplankton) and nannoplankton abundance (total occurrences per field of view (FOV)); percentage of benthic foraminifera (against total foraminifera); and core image of 364-M0077A-40R-1 0–110 cm (616.58–617.33 m below seafloor), with discrete trace fossils highlighted by arrows (see Extended Data Fig. 2 for a larger version of this image).

1 kyr, which is below the resolution of the method. With no sediment source other than settling of material suspended by the impact and subsequent tsunami and seiches, a more realistic estimate—based on Stokes' law—for the duration of this unit suggests about 6 years for the settling of a 2-μm grain of carbonate (an upper limit, as most grains are much larger; see Supplementary Information for further discussion).

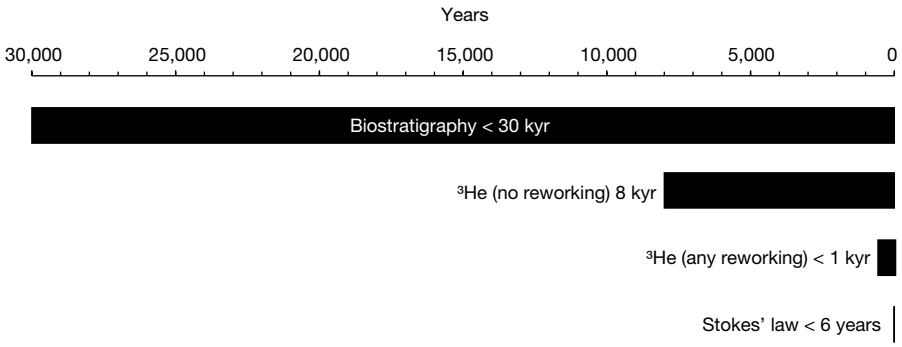


**Fig. 2 | Constraints on the age of the transitional unit.** Maximum durations of the transitional unit based on biostratigraphy (which suggests it was deposited in less than 30 kyr), extraterrestrial $^{3}$He (which suggests it was deposited in approximately 8 kyr if there is no reworking, or less than 1 kyr if there is any reworking) and Stokes' law, which suggests it was deposited in less than 6 years.

The lower portion of the overlying limestone, which contains fossils that appear approximately 30 kyr after the impact, appears conformable with the transitional unit and must therefore be condensed owing to low pelagic sedimentation in the first few tens of thousands of years after the impact.

Clear, discrete trace fossils, including *Planolites* and *Chondrites*, characterize the upper 20 cm of the transitional unit (above 54 cm) (Fig. 1 and Extended Data Fig. 2), providing unequivocal evidence for benthic life in the crater within years of the impact. Flattening of the structures indicates that the traces were formed while the sediment was still soft, during or shortly after the deposition of the transitional unit. Infilling of the burrows with brown, fine-grained micrite also suggests traces were syndepositional and not derived from mixing of the Danian limestone above the transitional unit. Trace fossils produced during deposition of the limestone, as indicated by light infilling material, are distinct and occur only in the uppermost few centimetres of the transitional unit (Extended Data Fig. 2).

The transitional unit microfossils are dominated by clearly reworked Maastrichtian foraminifera and nannoplankton, known across the Gulf of Mexico and Caribbean as the Cretaceous/Palaeogene (K/Pg) boundary cocktail[19] (Extended Data Fig. 3 and Supplementary Table 1). Although overall foraminiferal abundance (plotted as the number of foraminifera per gram of sedimentary rock; Fig. 1) is high at the base of the unit, species known to range across the boundary ('survivor species') are rare in the lower transitional unit and become more common up-section even as total foraminifera decline (Fig. 1). Survivor species, here defined as *G. cretacea*, *Muricohedbergella monmouthensis* and *Muricohedbergella holmdelensis*[20], dominate a depauperate assemblage in the upper 20 cm of the transitional unit, coinciding with the first appearance of trace fossils (Extended Data Figs. 4, 5).

The nannofossil assemblage in the transitional unit contains reworked Cretaceous specimens, including a group of clearly overgrown species (such as *Aspidolithus parcus* (also known as *Broinsonia parca*) and *Eiffellithus eximius*) that became extinct near the Campanian/Maastrichtian boundary. The remainder of the Cretaceous species, which dominate the assemblage, range to the top of or beyond the latest Maastrichtian age (Supplementary Table 2). Unusually small (less than 2 μm) and delicate specimens of *Micula* are observed throughout the transitional unit and increase in abundance up-section (Fig. 1), along with small *Retecapsa* (Extended Data Fig. 6). Taxa common at other sites of the earliest Danian stage are also present, including disaster genera (opportunistic groups that can tolerate high environmental stress) such as *Thoracosphaera* and *Braarudosphaera*. Unlike the foraminifera, there are no clear stratigraphic trends in overall nannoplankton abundance (Fig. 1).

Because survivor species lived both before and after the K/Pg mass extinction, it is impossible to determine for certain whether individual specimens in the transitional unit colonized the crater after the impact. However, the populations of foraminifera and nannoplankton are substantially different from those of the latest Cretaceous[12] (that is, the expected population if the whole assemblage was reworked), suggesting that these taxa were true survivors (Fig. 1 and Extended Data Fig. 6). *G. cretacea*, a common component of the survivor assemblage in the upper transitional unit, was restricted to marginal marine waters during the Maastrichtian and would not have been present at the pre-impact site, which was over 100 m deep[21] and over 500 km from shore[22]. The nannofossil assemblage in the transitional unit is considerably different from typical latest Maastrichtian assemblages, with some genera over-represented (*Watznaueria* and *Retecapsa*) and others under-represented (*Eiffellithus*, not including *E. eximius*, *Arkhangelskiella*, *Chiastozygus* and *Prediscosphaera*) (Extended Data Fig. 6). Additionally, *Micula*—a robust taxon often used as a proxy for dissolution—is not as abundant as elsewhere, indicating that these unusual abundances are not due to poor or selective preservation (Extended Data Fig. 6).

This initial appearance of life is notably fast, especially because crater-specific factors do not seem to have had a negative effect on the local recovery of life. A vigorous, high-temperature hydrothermal system was established within the crater and may have persisted for millions of years after the impact[23], especially across the peak ring where rocks exhumed from deep in the crust were extensively fractured[7]. Nevertheless, the appearance of burrowing organisms within years of the impact indicates that the hydrothermal system did not adversely affect seafloor life. Impact-generated hydrothermal systems are hypothesized to be potential habitats for early life on Earth[24] and on other planets, particularly below the surface. However, for marine impact craters in open ocean communication, such as Chicxulub (Extended Data Fig. 1), our data indicate that locally substantial but comparatively small volumes of hydrothermal fluids were overwhelmed by the $1.3 \times 10^4$ km$^3$ of well-mixed ocean water that filled the basin.

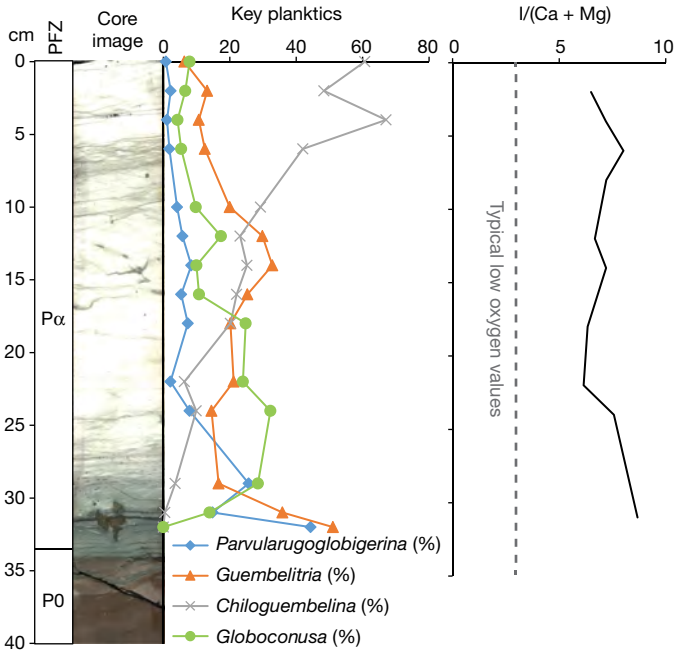


**Fig. 3 | Early Danian foraminifer abundances and I/(Ca + Mg) oxygenation proxy.** Left plot, Key Danian planktic foraminifera. Normal perforate planktic foraminifera (*Eoglobigerina*, *Globanomalina*, *Parasubbotina* and *Praemurica*) are rare throughout the study interval and not plotted here; all are plotted as a percentage of total planktic foraminifera. Right plot, I/(Ca + Mg) redox proxy, indicating well-oxygenated conditions in the Chicxulub crater through this interval. PFZ, planktic foraminifer zone.

Likewise, the open connection with the Gulf of Mexico prevented the development of anoxia in the crater. Our analyses of I/Ca ratios suggest that local dissolved oxygen was high and stable in Zone Pα (Fig. 3). This is in contrast to the smaller (85-km wide) Eocene Chesapeake Bay impact crater, where anoxia due to restriction is attributed as the cause of delayed recovery of the benthic ecosystem on the crater floor[25]. This comparison suggests that the establishment of life within marine impact craters is controlled more by circulation (and thus crater geometry) than by the magnitude of the impact or global environmental effects.

The overlying pelagic limestone, which was deposited within Zone Pα (30–200 kyr after the impact) contains abundant evidence of high productivity in a thriving ecosystem. The assemblage of planktic foraminifera in Zone Pα is diverse and abundant (Fig. 3). Good preservation in the lowermost sample (34 cm core depth) enabled the identification of over 60 species of benthic foraminifera, and benthics make up 12% of the total foraminiferal assemblage at this level (Supplementary Table 1). This percentage of benthics[26] and the overall benthic assemblage[27] are both typical of a palaeo-water depth of about 600–700 m (around the boundary between the upper and middle bathyal zones)[10,27]. At the base of the white limestone, trace fossils increase in size, abundance and diversity relative to the underlying

transitional unit. The abundance and diversity of benthic organisms indicate that by about 30 kyr after the impact, seafloor conditions had returned to normal and sufficient organic matter flux existed to sustain a diverse, multilayer benthic community.

Conversely, the nannoplankton assemblage in the Danian limestone is dominated by *Braarudosphaera* and calcareous dinoflagellate cysts (for example, *Thoracosphaera*), which are common disaster taxa in the early recovery interval. Large, foraminifer-sized calcispheres appear after about 100 kyr. Calcareous phytoplankton in the earliest Danian clearly represent a low-diversity, high-productivity bloom. Genera such as *Neobiscutum* and *Prinsius*, which are common bloom taxa in the recovery interval at other Northern Hemisphere sites, do not become common until several metres higher in the section, over one million years after the impact. Organic microfossils are completely absent from the study interval, probably owing to poor preservation of organic material.

Geochemical palaeoproductivity proxies, particularly Ba/Ti and Ba/Fe ratios, also indicate high productivity in the post-impact Danian limestone (Fig. 1). Ba/Ti ratios of about 1.0 at the base of the limestone (approximately 30 kyr after the impact) and about 2.0 above that (15 cm higher, or about 100 kyr after the impact) indicate relatively high and increasing productivity in the Chicxulub basin in the earliest Danian.

The recovery of productivity in the crater is faster than that at many sites, including those in the Gulf of Mexico, some of which took 300 kyr or more to recover to a similar extent[8,11]. Therefore, we find that proximity to the impact was not a control on recovery in marine ecosystems. The wide range of rates of recovery in the oceans show no relationship with geographic distance to the crater and so are best explained by natural ecological interactions, such as incumbency and competitive exclusion, between organisms within recovery ecosystems[8,14]. These trends can be used to understand the rates of recovery after other major extinction events and to predict the long-term recovery of modern ecosystems affected by pollution and climate change.

## Online content

Any Methods, including any statements of data availability and Nature Research reporting summaries, along with any additional references and Source Data files, are available in the online version of the paper at https://doi.org/10.1038/s41586-018-0163-6.

Received: 27 October 2017; Accepted: 3 April 2018;
Published online: 30 May 2018

1. Jablonski, D. in *Extinction Rates* (eds Lawton, J. H. & May, R. M.) 25–44 (Oxford Univ. Press, Oxford, 1995).
2. Schulte, P. et al. The Chicxulub asteroid impact and mass extinction at the Cretaceous–Paleogene boundary. *Science* **327**, 1214–1218 (2010).
3. Alvarez, L. W., Alvarez, W., Asaro, F. & Michel, H. V. Extraterrestrial cause for the Cretaceous–Tertiary extinction. *Science* **208**, 1095–1108 (1980).
4. Smit, J. & Hertogen, J. An extraterrestrial event at the Cretaceous–Tertiary boundary. *Nature* **285**, 198–200 (1980).
5. Renne, P. R. et al. Time scales of critical events around the Cretaceous–Paleogene boundary. *Science* **339**, 684–687 (2013).
6. Hildebrand, A. R. et al. Chicxulub crater: a possible Cretaceous/Tertiary boundary impact crater in the Yucatán Peninsula, Mexico. *Geology* **19**, 867–871 (1991).
7. Morgan, J. V. et al. The formation of peak rings in large impact craters. *Science* **354**, 878–882 (2016).
8. Hull, P. M. & Norris, R. D. Diverse patterns of ocean export productivity change across the Cretaceous–Paleogene boundary: new insights from biogenic barium. *Paleoceanography* **26**, PA3205 (2011).
9. Alegret, L. & Thomas, E. Cretaceous/Paleogene boundary bathyal paleoenvironments in the central North Pacific (DSDP site 465), the northwestern Atlantic (ODP site 1049), the Gulf of Mexico, and the Tethys: the benthic foraminiferal record. *Palaeogeogr. Palaeoclimatol. Palaeoecol.* **224**, 53–82 (2005).
10. Alegret, L., Molina, E. & Thomas, E. Benthic foraminifera at the Cretaceous–Tertiary boundary around the Gulf of Mexico. *Geology* **29**, 891–894 (2001).
11. Alegret, L., Arenillas, I., Arz, J. A. & Molina, E. Foraminiferal event-stratigraphy across the Cretaceous/Paleogene boundary. *Neues Jahrb. Geol. Paläontol. Abh.* **231**, 25–50 (2004).
12. Jiang, S., Bralower, T. J., Patzkowsky, M. E., Kump, L. R. & Schueth, J. D. Geographic controls on nannoplankton extinction across the Cretaceous/Palaeogene boundary. *Nat. Geosci.* **3**, 280–285 (2010).
13. Solé, R. V., Montoya, J. M. & Erwin, D. H. Recovery after mass extinction: evolutionary assembly in large-scale biosphere dynamics. *Philos. Trans. R. Soc. Lond. B* **357**, 697–707 (2002).
14. Schueth, J. D., Bralower, T. J., Jiang, S. & Patzkowsky, M. E. The role of regional survivor incumbency in the evolutionary recovery of calcareous nannoplankton from the Cretaceous/Paleogene (K/Pg) mass extinction. *Paleobiology* **41**, 661–679 (2015).
15. Hull, P. M. Norris, R.D., Bralower, T. J. & Schueth, J.D. A role for chance in marine recovery from the end-Cretaceous extinction. *Nat. Geosci.* **4**, 856–860 (2011).
16. Yedid, G., Ofria, C. A. & Lenski, R. E. Selective press extinctions, but not random pulse extinctions, cause delayed ecological recovery in communities of digital organisms. *Am. Nat.* **173**, E139–E154 (2009).
17. Gulick, S., Morgan, J., Mellett, C. L. & the Expedition 364 Scientists. *Expedition 364 Preliminary Report: Chicxulub: Drilling the K-Pg Impact Crater* (International Ocean Discovery Program, College Station, TX, 2017).
18. Wade, B. S., Pearson, P. N., Berggren, W. A. & Pälike, H. Review and revision of Cenozoic tropical planktonic foraminiferal biostratigraphy and calibration to the geomagnetic polarity and astronomical time scale. *Earth Sci. Rev.* **104**, 111–142 (2011).
19. Bralower, T. J., Paull, C. K. & Leckie, R. M. The Cretaceous–Tertiary boundary cocktail: Chicxulub impact triggers margin collapse and extensive sediment gravity flows. *Geology* **26**, 331–334 (1998).
20. Olsson, D. K., Hemleben, C., Berggren, W. A. & Huber, B. T. *Atlas of Paleocene Planktonic Foraminifera* (Smithsonian Institution, Washington, 1999).
21. Gulick, S. P. S. et al. Importance of pre-impact crustal structure for the asymmetry of the Chicxulub impact crater. *Nat. Geosci.* **1**, 131–135 (2008).
22. Sohl, N. F., Martínez, E. R., Salmerón-Ureña, P. & Soto-Jaramillo, F. in *Geology of North America, Volume J: Gulf of Mexico Basin* (ed. Salvador, A.) 205–244 (Geological Society of America, Boulder, 1991).
23. Abramov, O. & Kring, D. A. Numerical modeling of impact-induced hydrothermal activity at the Chicxulub crater. *Meteorit. Planet. Sci.* **42**, 93–112 (2007).
24. Cockell, C. S. The origin and emergence of life under impact bombardment. *Phil. Trans. R. Soc. Lond. B* **361**, 1845–1856 (2006).
25. Poag, C. W. in *The ICDP-USGS Deep Drilling Project in the Chesapeake Bay Impact Structure: Results from the Eyreville Core Holes (The Geological Society of America Special Paper 458)* (eds Gohn, G. S. et al.) 747–773 (Geological Society of America, Boulder, 2009).
26. Leckie, R. M. & Olson, H. C. In *Micropaleontologic Proxies for Sea-level Change and Stratigraphic Discontinuities (SEPM Special Publication 75)* (eds. Olson, H. C. & Leckie, R. M.) 5–19 (Society for Sedimentary Geology, Tulsa, 2003).
27. Alegret, L. & Thomas, E. Upper Cretaceous and lower Paleocene benthic foraminifera from northeastern Mexico. *Micropaleontology* **47**, 269–316 (2001).

**Acknowledgements** This research used samples and data provided by the International Ocean Discovery Program (IODP). IODP Expedition 364 was jointly funded by the European Consortium for Ocean Research Drilling (ECORD) and International Continental Drilling Program (ICDP), with contributions and logistical support from the Yucatán State Government and Universidad Nacional Autónoma de México (UNAM). We thank T. Cayton for assistance with crushing and washing samples; S. Dameron, R. Moura de Mello and M. Leckie for helpful discussions on benthic foraminifer taxonomy; J. Maner for assistance with the UT ESEM laboratory and R. Martindale for assistance with petrographic microscope imaging. We are particularly grateful for assistance of the staff of the IODP Core Repository in Bremen, Germany for their assistance taking these samples and running shipboard analyses. The authors acknowledge Post-Expedition Awards from the US Science Support Program for C.M.L. and T.J.B., NSF OCE 1737351, and NASA NNX16AJ60G. Funding for F.J.R.-T. was provided by Project CGL2015-66835-P (Secretaría de Estado de I+D+I, Spain), and Scientific Excellence Unit UCE-2016-05 (Universidad de Granada).

**Reviewer information** *Nature* thanks B. Huber and the other anonymous reviewer(s) for their contribution to the peer review of this work.

**Author contributions** All authors participated in sampling and data collection offshore and/or onshore during IODP–ICDP Expedition 364. C.M.L., T.J.B., F.J.R.-T., H.J. and J.S. collected and analysed microfossil data, M.T.W. provided detailed sedimentology, and J.D.O., P.C. and K.F. collected trace element, X-ray fluorescence and He isotope data, respectively. All authors contributed to writing and/or editing of the manuscript.

**Competing interests** The authors declare no competing interests.

**Additional information**
**Extended data** is available for this paper at https://doi.org/10.1038/s41586-018-0163-6.
**Supplementary information** is available for this paper at https://doi.org/10.1038/s41586-018-0163-6.
**Reprints and permissions information** is available at http://www.nature.com/reprints.
**Correspondence and requests for materials** should be addressed to C.M.L.
**Publisher's note:** Springer Nature remains neutral with regard to jurisdictional claims in published maps and institutional affiliations.

## METHODS

Sample size was determined according to standard community practice (collecting approximately 300 specimens per sample, when possible). No statistical methods were used to predetermine sample size. The experiments were not randomized and investigators were not blinded to allocation during experiments and outcome assessment.

The IODP–ICDP Expedition 364 drilled the peak ring of the Chicxulub crater in the spring of 2016 (Extended Data Fig. 1). Samples were taken at the Bremen IODP core repository during the Expedition 364 sampling party. Core depth in centimetres—with zero at the top of the section (616.24 m below sea floor)—are reported throughout. Core material was indurated, and ~0.5-cm quarter-rounds were cut out with a rock saw. Owing to the need to reserve core material for rare earth element geochemistry (data not shown), the lowermost ~1.5 cm of the Danian limestone was not sampled. Individual samples were subdivided for foraminifera, calcareous nannoplankton and discrete geochemical analyses.

Forty-three samples were examined for planktic and benthic foraminifera from core 40 from 0–110 cm depth. Samples were weighed, crushed with a mortar and pestle, soaked overnight (or longer) in a 10% solution of hydrogen peroxide buffered with borax and washed over a 43-μm sieve to ensure capture of small Danian taxa. The sieve was soaked in methylene blue dye between samples to identify contaminated specimens. Samples were then dried in an oven, split to obtain a manageable volume of material, and examined for foraminifera, calcispheres, and other sand-sized particles. In the Danian limestone, at least 300 specimens were counted to establish a statistically robust population[28] and the rest of the residue was then examined for biostratigraphically important taxa. Low abundances in the transitional unit precluded 300-specimen counts. However, we demonstrate that our values are sufficient to reject the null hypothesis (that the observed enrichments in survivor taxa are the result of random noise) with binomial confidence limits. This calculation traditionally provides the basis for the 300-specimen 'rule': counting 300 specimens provides statistical confidence at a 95% confidence interval that a species that makes up 1% of the population is represented in the count[28]. As we show, fewer specimens are sufficient to demonstrate the presence of a survivor population in our samples. Binomial confidence limits for samples with fewer than 300 specimens are reported in Supplementary Table 1. Additionally, a single unusually well-preserved sample at the base of the post-impact limestone was examined for rare benthic species to determine the true diversity of benthic foraminifera at the base of the unit (Supplementary Table 1). Planktic foraminifer biozonation follows the P zones of Berggren and Pearson[29] as modified by Wade et al.[18].

Ninety-seven samples were examined for nannofossils. Samples were disaggregated in water, and smear slides were made from the supernatant. Slides were observed in a transmitted light microscope at 1,600× until at least 100 specimens were observed (Supplementary Table 2). Standard taxonomy was applied (http://www.mikrotax.org/Nannotax3/index.php?dir=Coccolithophores). The abundance of taxa at site M0077 was compared to a previous compilation of global K/Pg nannoplankton[12].

Ichnological analysis was conducted from 0–110 cm. Ichnological observations were conducted on core material and a detailed and continuous analysis of digital images. To improve visibility of ichnological features, images were treated by a digital image methodology, based on the modification of image adjustments as levels, brightness and vibrance[30,31]. Ichnotaxonomical classification of trace fossils was based on the overall shape and the presence of diagnostic criteria such as size and presence of branches[32]. Special attention was given to the infilling material of biogenic structures.

The measurement of I/(Ca + Mg) was carried out using a procedure similar to a previously described method[33]. For each sample and geostandard, approximately 3–4 mg of carbonate powder was weighed out, dissolved in ~0.45 M nitric solution and then diluted using 0.1 M nitric acid and 0.5% TMAH solution. All reported measurements are from samples that had a matrix of 50 ± 5 p.p.m. calcium solution to ensure the most precise iodine measurement. Dissolved samples had TMAH solution added within an hour to avoid any possible loss of volatilized iodine[33]. Samples were measured using an Agilent inductively coupled plasma mass spectrometer 7500 cs housed within the geochemistry group of the National High Magnetic Field Laboratory at Florida State University. A previously reported known sample, Key Largo (KL 1-1) was used to ensure reliable reproducibility. Our value of 5.51 μmol/mol was within error of the reported value of 5.55 μmol/mol. A previous study[34] found that generally low oxygen conditions correspond to ~2.6 μmol/mol for I/(Ca + Mg). Values are reported in Supplementary Table 3.

Section 1 of core 40 was scanned with an AVAATECH XRF Core Scanner II at MARUM (Bremen, Germany) during the onshore phase of Expedition 364 (Fig. 1). The split core was covered with a 4-μm-thick SPEX CertiPrep Ultralene foil to avoid contamination. X-ray fluorescence data were acquired with a Canberra X-PIPS silicon drift detector with 1550 eV resolution, a Canberra DAS 1000 digital spectrum analyser and an Oxford Instruments 50 W XTF011 X-ray tube with rhodium target material. X-ray spectra were processed with WIN AXIL software from Canberra Erisys at a resolution of 12 mm and a step of 10 mm. Scans were conducted at different voltages to determine a range of element concentrations: 50 kV, with a beam current of 1 mA (Ba and Sr; average dead time of 5%), and 10 kV with a beam current of 0.15 mA (Al, Si, K, Ca, Ti, Fe, Mn and S; average dead time of 11%). For each scan, sampling time was 20 s per spot.

$^3$He is delivered to the Earth's surface by cosmic dust grains and over short time spans (about one million years) can be used as a constant flux proxy[35]. Previous work has shown that the K/Pg impactor was not associated with enhanced $^3$He flux, and the mean extraterrestrial $^3$He flux from cosmic dust accretion at the end of the Cretaceous ($106 \times 10^{-15}$ cc (standard temperature and pressure) per g per cm$^2$ per kyr) was used to estimate the duration over which the K/Pg boundary clay was deposited at Gubbio and El Kef[36]. We use a similar approach here to establish the sedimentation rate of the transitional unit, which we use to develop an age model.

Helium isotope ratios and concentrations were measured on ~1-g aliquots of sediment following standard analytical procedures[31]. Extraterrestrial $^3$He concentrations were computed from measured He isotopic compositions using an isotopic deconvolution model[36]. Results are shown in Extended Data Table 1. $^3$He concentrations and $^3$He/$^4$He ratios are generally low compared to typical marine sediments of similar age[37,38]. Nevertheless, with the exception of the lowest sample in the transitional unit (106.5 cm), the fraction of $^3$He attributable to an extraterrestrial source is high, ranging from ~0.70 to 0.96. The deepest sample has a similar $^3$He concentration to other samples in the transitional unit, but ~5 times more $^4$He. This elevated $^4$He probably arises from a higher concentration of terrigenous $^4$He-bearing material deposited rapidly after the impact.

We see no evidence for extraterrestrial He carried in impactor fragments, such as highly elevated and/or highly variable $^3$He and $^3$He/$^4$He ratios. The absence of such a signal is consistent with either (a) the absence of impactor fragments in the material analysed or (b) the loss of extraterrestrial $^3$He from the impactor via heating, vaporization or fusion. Note that, unlike many tracers of the impactor (such as Ir), deposition of fused or vaporized impactor will leave no trace in the sedimentary record because once He is lost into the atmosphere, it can no longer be retained in sediments.

**Reporting summary.** Further information on experimental design is available in the Nature Research Reporting Summary linked to this paper.

**Data availability.** X-ray fluorescence data have previously been published[39] and are available online (https://doi.org/10.14379/iodp.proc.364.2017). All other data supporting the findings of this study are available within the paper and its Supplementary Information.


28. Buzas, M. A. Another look at confidence limits for species proportions. *J. Paleontol.* **64**, 842–843 (1990).
29. Berggren, W. A. & Pearson, P. N. A revised tropical and subtropical Paleogene planktonic foraminiferal zonation. *J. Foraminiferal Res.* **35**, 279–298 (2005).
30. Dorador, J. & Rodríguez-Tovar, F. Digital image treatment applied to ichnological analysis of marine core sediments. *Facies* **60**, 39–44 (2014).
31. Dorador, J. & Rodríguez-Tovar, F. J. Stratigraphic variation in ichnofabrics at the "Shackleton Site" (IODP Site U1385) on the Iberian Margin: paleoenvironmental implications. *Mar. Geol.* **377**, 118–126 (2016).
32. Knaust, D. *Atlas of Trace Fossils in Well Core: Appearance, Taxonomy and Interpretation* (Springer, New York, 2017).
33. Lu, Z., Jenkyns, H. C. & Rickaby, R. E. M. Iodine to calcium ratios in marine carbonate as a paleo-redox proxy during oceanic anoxic events. *Geology* **38**, 1107–1110 (2010).
34. Hardisty, D. S. et al. Perspectives on Proterozoic surface ocean redox from iodine contents in ancient and recent carbonate. *Earth Planet. Sci. Lett.* **463**, 159–170 (2017).
35. Farley, K. A. & Eltgroth, S. F. An alternative age model for the Paleocene–Eocene thermal maximum using extraterrestrial $^3$He. *Earth Planet. Sci. Lett.* **208**, 135–148 (2003).
36. Patterson, D. B. & Farley, K. A. Extraterrestrial $^3$He in seafloor sediments: evidence for correlated 100 kyr periodicity in the accretion rate of interplanetary dust, orbital parameters, and Quaternary climate. *Geochim. Cosmochim. Acta* **62**, 3669–3682 (1998).
37. Mukhopadhyay, S. Farley, K. A. & Montanari, A. A 35 Myr record of helium in pelagic limestones from Italy: implications for interplanetary dust accretion from the early Maastrichtian to the middle Eocene. *Geochim. Cosmochim. Acta* **65**, 653–669 (2001).
38. Mukhopadhyay, S., Farley, K. A. & Montanari, A. A short duration of the Cretaceous-Tertiary boundary event: evidence from extraterrestrial helium-3. *Science* **291**, 1952–1955 (2001).
39. Morgan, J., Gulick, S., Mellet, C.L., Green, S.L. & Expedition 364 Scientists. *Chicxulub: Drilling the K-Pg Impact Crater. Proceedings of the International Ocean Discovery Program 364* (International Ocean Discovery Program, College Station, 2017).

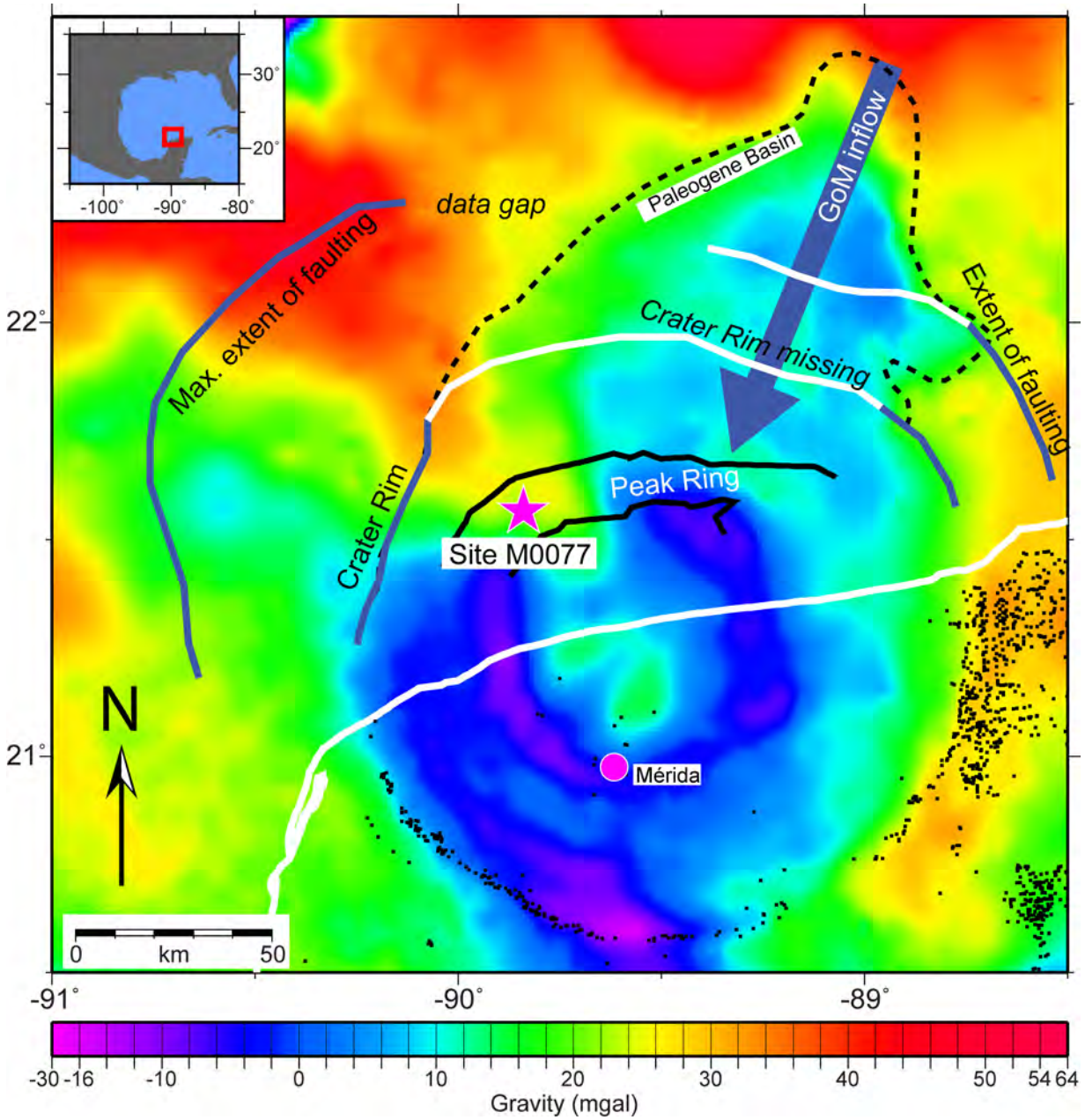


**Extended Data Fig. 1 | Location of site M0077 in the Chicxulub crater as seen using gravity data.** Black dots are cenotes. Modified from Gulick et al. [21].

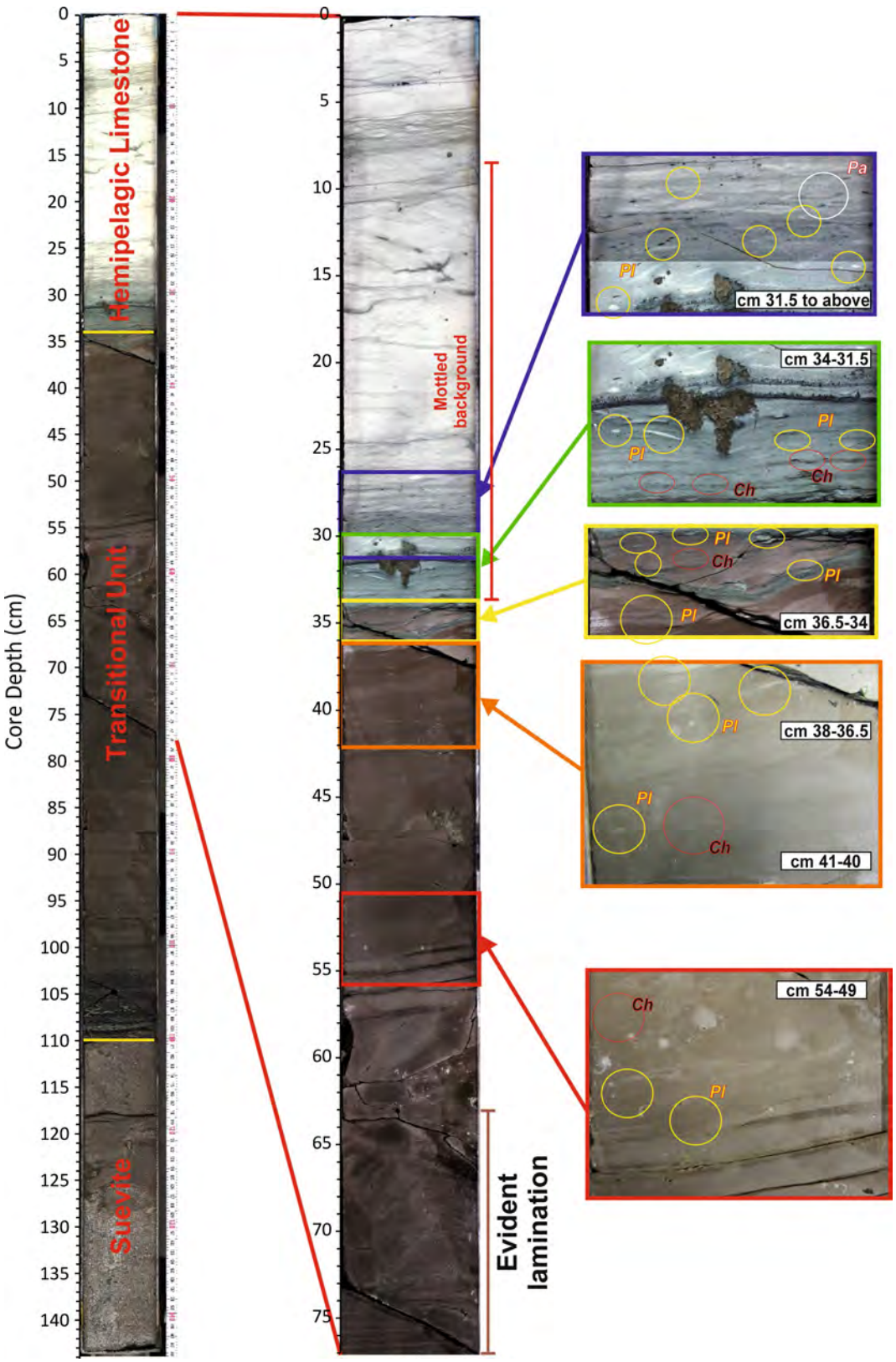


**Extended Data Fig. 2 | Trace fossils in core 40 section 1 of IODP hole M0077A.** Discrete burrows in the upper transitional unit and the lower limestone are circled and labelled by the genus. Above the base of the limestone, trace fossils are abundant; representative examples are highlighted in the lower 10 cm of this interval. Ch, *Chondrites*; Pl, *Planolites*; Pa, *Palaeophycus*.

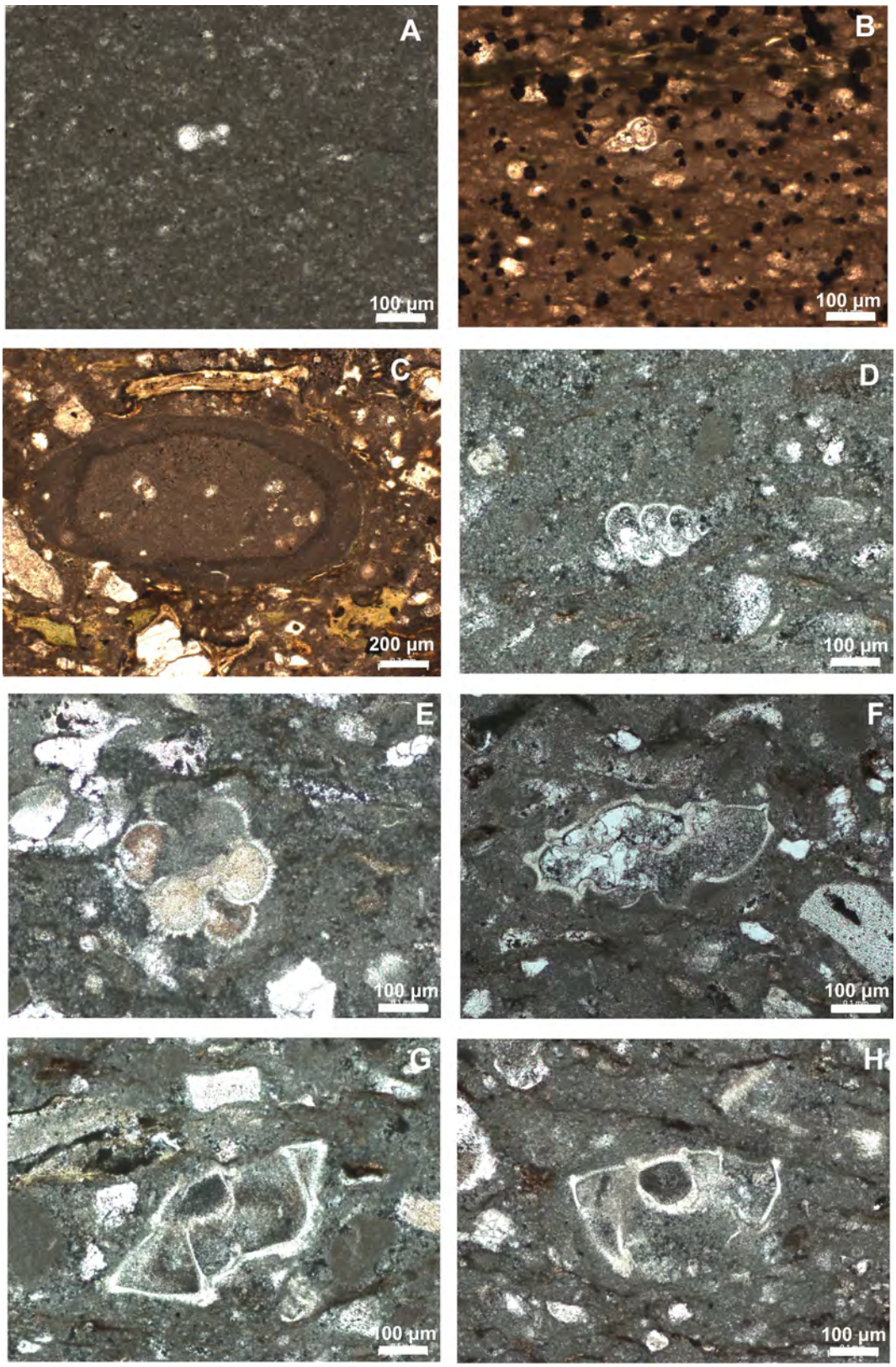


**Extended Data Fig. 3 | Reworked Cretaceous foraminifera in the transitional unit. a**, *Globigerinelloides* sp., sample 364-M0077A-40R-1-W, 55–56 cm. **b**, *Heterohelix* sp., sample 364-M0077A-40R-1-W, 104–105 cm. **c**, Clast of pelagic limestone containing older Cretaceous planktic foraminifera, sample 364-M0077A-40R-1-W, 106–110 cm. **d**, *Praegublerina pseudotessera*, sample 364-M0077A-40R-1-W, 118–129 cm. **e**, *Racemiguembelina powelli*, sample 364-M0077A-40R-1-W, 118–129 cm. **f**, *Globotruncana bulloides*, sample 364-M0077A-40R-1-W, 110–118 cm. **g**, *Globotruncanita stuartiformis*, sample 364-M0077A-40R-1-W, 118–129 cm. **h**, *Globotruncanita elevata*, sample 364-M0077A-40R-1-W, 118–129 cm. Scale bars, 100 µm.

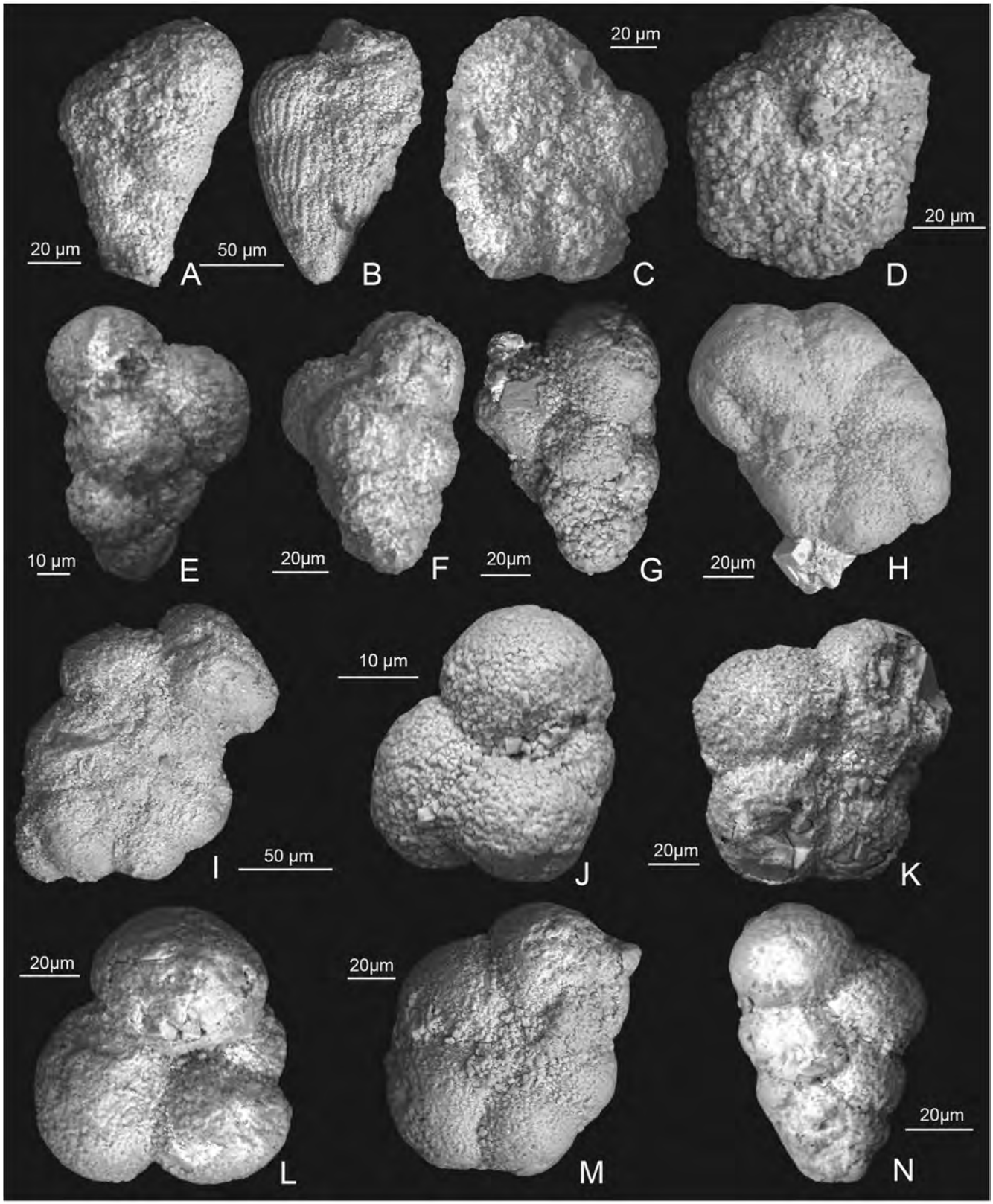


**Extended Data Fig. 4 | Scanning electron micrographs of planktic foraminifera from core 40. a**, **b**, Examples of common reworked Cretaceous biserials, sample 364-M0077A-40R-1, 102–103 cm. **c**, *Muricohedbergella monmouthensis*, sample 364-M0077A-40R-1-W, 102–103 cm. **d**, *Muricohedbergella holmdelensis*, sample 364-M0077A-40R-1-W, 44–45 cm. **e**, *Guembelitria cretacea*, sample 364-M0077A-40R-1-W, 44–45 cm. **f**, *G. cretacea*, sample 364-M0077A-40R-1-W, 29–30 cm. **g**, *G. cretacea*, sample 364-M0077A-40R-1-W, 29–30 cm. **h**, *Parvularugoglobigerina eugubina* 364-M0077A-40R-1-W, 31–32 cm. **i**, *P. eugubina*, sample 364-M0077A-40R-1-W, 31–32 cm. **j**, *Globoconusa daubjergensis*, sample 364-M0077A-40R-1-W, 31–32 cm. **k**, *Eoglobigerina eobulloides*, sample 364-M0077A-40R-1-W, 29–30 cm. **l**, *Eoglobigerina edita*, sample 364-M0077A-40R-1-W, 29–30 cm. **m**, *Praemurica taurica*, sample 364-M0077A-40R-1-W, 10–11 cm. **n**, *Chiloguembelina morsei*, sample 364-M0077A-40R-1-W, 10–11 cm.

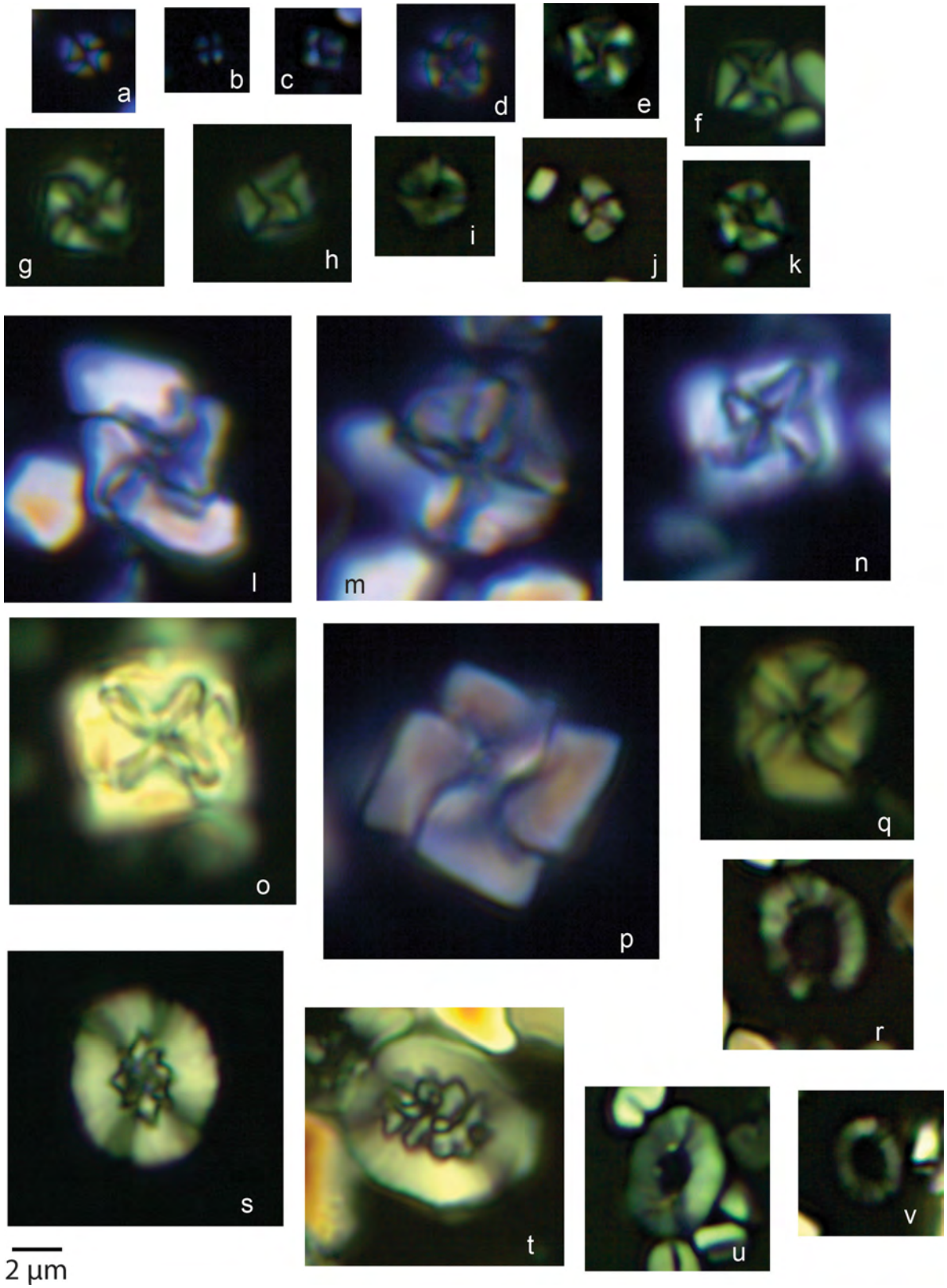


**Extended Data Fig. 5 | Small and regular-sized nannofossils in the transitional unit.** All photographs from core 364-M0077-40R-1-W. Measurements in centimetres refer to depth in section 1 of core 40. **a**–**k**, Images of small *Micula* spp.: **a**, 55–56 cm; **b**, 41–42 cm; **c**, 95–96 cm; **d**, 41–42 cm; **e**, 90–91 cm; **f**, 94–95 cm; **g**, 91–92 cm; **h**, 91–92 cm; **i**, 45–46 cm; **j**, 100–101 cm; **k**, 81–82 cm. **l**–**q**, Images of regular-sized *Micula* spp.: **l**, 44–45 cm; **m**, 41–42 cm; **n**, 51–52 cm; **o**, 105–106 cm; **p**, 97–98 cm; **q**, 36–37 cm. **s**, **t**, Images of regular-sized *Retecapsa* spp.: **s**, 85–86 cm; **t**, 100–101 cm. **r**–**v**, Images of small *Retecapsa* spp.: **r**, 100–101 cm; **u**, 71–72 cm, **v**, 100–101 cm. Scale bar, 2 µm.

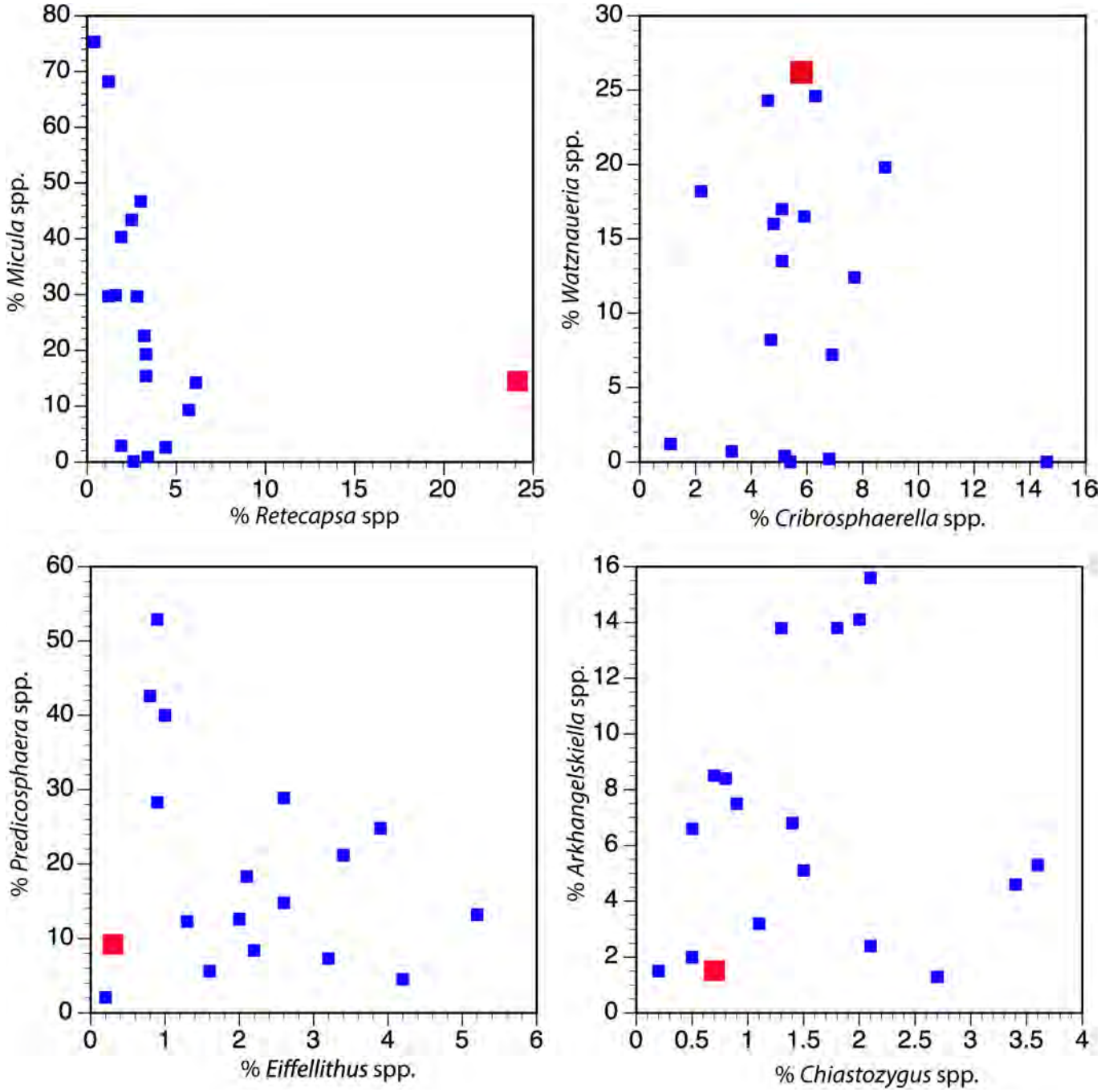


**Extended Data Fig. 6 | Relative abundances of major Maastrichtian calcareous nannoplankton.** Small blue squares are Maastrichtian sites from a global compilation[12]; larger red squares are from the transitional unit at site M0077. These data demonstrate the unusual abundance of *Watznaueria* and *Retecapsa* at site M0077.

**Extended Data Table 1 | $^{3}$He data**

| Sample | start cm | stop cm | $^{3}$He pcc/g | $^{4}$He ncc/g | Absolute $^{3}$He/$^{4}$He | Fraction $^{3}$He ET | Maximum $^{3}$He -Based Model Age (kyr) |
|---|---|---|---|---|---|---|---|
| KT39 | 39 | 40 | 0.0068 | 13.6 | 5.04E-07 | 0.96 | 6.0 |
| KT48 | 48 | 49 | 0.0055 | 35.4 | 1.56E-07 | 0.87 | 4.9 |
| KT59 | 59 | 60 | 0.0064 | 23.1 | 2.78E-07 | 0.92 | 4.0 |
| KT68 | 68 | 69 | 0.0042 | 31.6 | 1.33E-07 | 0.84 | 2.9 |
| KT79 | 79 | 80 | 0.0036 | 18.3 | 1.99E-07 | 0.9 | 1.9 |
| KT89 | 89 | 90 | 0.0105 | 34.7 | 3.04E-07 | 0.93 | 0.9 |
| KT99 | 99 | 100 | 0.0045 | 64.3 | 6.99E-08 | 0.70 | 0.1 |
| KT106.5 | 107 | 108 | 0.0109 | 327 | 3.32E-08 | 0.37 | 0.0 |